Title

Cell contact guidance via sensing anisotropy of network mechanical resistance

Journal

Proceedings of the National Academy of Sciences of the United States of America, 118(29)

ISSN

0027-8424

Authors

Thrivikraman, Greeshma
Jagiełło, Alicja
Lai, Victor K
et al.

Publication Date

2021-07-20

DOI

10.1073/pnas.2024942118

Peer reviewed

Cell contact guidance via sensing anisotropy of network mechanical resistance

Greeshma Thrivikraman[a], Alicja Jagiełło[b], Victor K. Lai[c], Sandra L. Johnson[a], Mark Keating[b], Alexander Nelson[a], Billianne Schultz[a], Connie M. Wang[d], Alex J. Levine[e,f,g], Elliot L. Botvinick[b,h,i], and Robert T. Tranquillo[a,d,1]

[a]Department of Biomedical Engineering, University of Minnesota, Twin Cities, Minneapolis, MN 55455; [b]Department of Biomedical Engineering, University of California, Irvine, CA 92617; [c]Department of Chemical Engineering, University of Minnesota, Duluth, MN 55812; [d]Department of Chemical Engineering and Materials Science, University of Minnesota, Twin Cities, Minneapolis, MN 55455; [e]Department of Chemistry and Biochemistry, University of California, Los Angeles, CA 90095; [f]Department of Physics & Astronomy, University of California, Los Angeles, CA 90095; [g]Department of Computational Medicine, University of California, Los Angeles, CA 90095; [h]Beckman Laser Institute and Medical Clinic, University of California, Irvine, CA 92612; and [i]The Edwards Lifesciences Center for Advanced Cardiovascular Technology, University of California, Irvine, CA 92617

Edited by David A. Weitz, Harvard University, Cambridge, MA, and approved June 1, 2021 (received for review December 6, 2020)

Despite the ubiquitous importance of cell contact guidance, the signal-inducing contact guidance of mammalian cells in an aligned fibril network has defied elucidation. This is due to multiple interdependent signals that an aligned fibril network presents to cells, including, at least, anisotropy of adhesion, porosity, and mechanical resistance. By forming aligned fibrin gels with the same alignment strength, but cross-linked to different extents, the anisotropic mechanical resistance hypothesis of contact guidance was tested for human dermal fibroblasts. The cross-linking was shown to increase the mechanical resistance anisotropy, without detectable change in network microstructure and without change in cell adhesion to the cross-linked fibrin gel. This methodology thus isolated anisotropic mechanical resistance as a variable for fixed anisotropy of adhesion and porosity. The mechanical resistance anisotropy $|Y^*|^{-1} - |X^*|^{-1}$ increased over fourfold in terms of the Fourier magnitudes of microbead displacement $|X^*|$ and $|Y^*|$ at the drive frequency with respect to alignment direction Y obtained by optical forces in active microrheology. Cells were found to exhibit stronger contact guidance in the cross-linked gels possessing greater mechanical resistance anisotropy: the cell anisotropy index based on the tensor of cell orientation, which has a range 0 to 1, increased by 18% with the fourfold increase in mechanical resistance anisotropy. We also show that modulation of adhesion via function-blocking antibodies can modulate the guidance response, suggesting a concomitant role of cell adhesion. These results indicate that fibroblasts can exhibit contact guidance in aligned fibril networks by sensing anisotropy of network mechanical resistance.

contact guidance | aligned fibril networks | mechanical resistance anisotropy | fibroblasts

Contact guidance refers to the tendency of a cell to orient and migrate bidirectionally in response to anisotropic topographical features, such as parallel grooves on a two-dimensional (2D) substratum or aligned fibrils in a three-dimensional (3D) collagen or fibrin gel. Contact guidance has been ascribed importance in a number of physiological processes since Weiss first identified and investigated its role in development (1). More recently, the role of contact guidance in cancer metastasis (2) as well as tissue engineering scaffold design (3) has been described.

Contact guidance on 2D substrata like parallel grooves or adhesive ligand stripes has been intensively studied (recent examples include refs. 4–6) because in these experiments, the guidance field can be precisely defined and easily manipulated. However, it is the case of aligned fibrils that has the preponderance of physiological relevance. Contact guidance is also vital to the success of engineered connective tissues that mimic native alignment (and thereby function) by harnessing mechanically constrained fibrin gel compaction by fibroblasts and the associated contact guidance response (7–9). Unfortunately, even for the case of collagen and fibrin gels, not to mention tissues, the guidance field generally cannot be precisely defined or controllably manipulated. This is because of the inherent biophysical complexities of an aligned fibril network, resulting in multiple interdependent and simultaneous signals presented to cells. These signals include anisotropy of adhesion, porosity, and mechanical resistance (a combination of elastic stiffness and viscous friction, in general), at least. In a recent publication on this topic (10), for example, a correlation was suggested between protrusion activity with respect to alignment direction and contact guidance. This study made use of varied gel concentrations (typical for contact guidance studies), a method that confounds easy interpretation because all potential anisotropies are almost certainly altered simultaneously.

While there are phenomenological studies reporting the contact guidance response of cells in aligned collagen and fibrin gels (11–14), the signal-inducing contact guidance in aligned fibrils has thus far defied elucidation since Dunn first proposed contact guidance in response to these anisotropies nearly 40 y ago (15), illustrated in Fig. 1. The main reason for the lack of progress in distinguishing between these anisotropies is the intrinsic difficulty in changing just one of them in an aligned fibril network—in Dunn's terms: chemical anisotropy, mechanical anisotropy, or steric anisotropy—without changing the others. This stands in stark contrast to almost every other form of directed cell migration

Significance

Cell contact guidance in aligned fibers is, in many ways, a final frontier in directed cell migration. Despite its ubiquitous importance in normal/pathological processes, notably metastasis from solid tumors, and scaffold design for tissue engineering/regenerative medicine, the signal that induces contact guidance in an aligned fiber network has defied elucidation. We report definitive demonstration of a biophysical signal sensed by fibroblasts cultured within aligned fibrils: mechanical resistance anisotropy, the resistance resulting from viscous and elastic properties of fibril network to pseudopod protrusion/retraction and how it differs in different directions (anisotropy). This discovery is of fundamental importance to understanding contact guidance, providing a rationale, currently lacking, for future studies of the intracellular signal transduction/response pathways for physiologically relevant contact guidance.

Author contributions: G.T., A.J., E.L.B., and R.T.T. designed research; G.T., A.J., V.K.L., S.L.J., M.K., A.N., and C.M.W. performed research; B.S. contributed new reagents/analytic tools; G.T., A.J., V.K.L., S.L.J., M.K., A.N., A.J.L., E.L.B., and R.T.T. analyzed data; and G.T., A.J., E.L.B., and R.T.T. wrote the paper.

The authors declare no competing interest.

This article is a PNAS Direct Submission.

[1]To whom correspondence may be addressed. Email: tranquillo@umn.edu.

This article contains supporting information online at https://www.pnas.org/lookup/suppl/doi:10.1073/pnas.2024942118/-/DCSupplemental.

Published July 15, 2021.

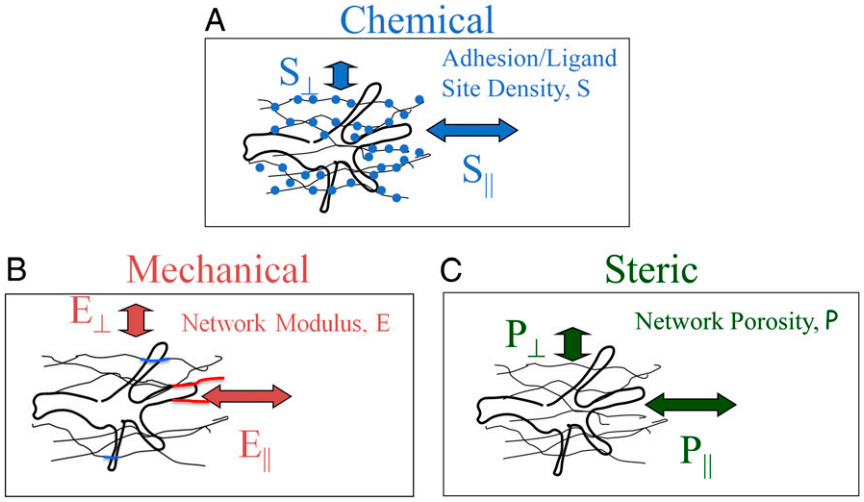

Fig. 1. Illustration of Dunn's hypotheses for the signal-inducing cell contact guidance in aligned fibrils. A cell with four pseudopods is depicted. (*A*) Chemical (adhesion) anisotropy. Cell-binding sites are indicated by blue dots. (*B*) Mechanical (stiffness/friction) anisotropy. Fibrils presenting a high local modulus to the pseudopod because of their coalignment are colored red, and fibrils presenting a local low modulus to the pseudopods because of their anti-alignment are colored blue. The colored segments are also thickened for visualization. (*C*) Steric (porosity) anisotropy. Note this figure is not drawn to scale for clarity; as we (59) and others (e.g., ref. 60) have shown with electron microscopy, a pseudopod is much larger than the typical pore size in the standard in vitro models (collagen and fibrin gels) and interacts with many interconnected fibrils simultaneously, not single fibrils.

in which the signal is absolutely clear, for example, a chemotactic factor concentration gradient in chemotaxis, an adhesion gradient in haptotaxis, an electric potential gradient in galvanotaxis, and a stiffness gradient in durotaxis.

Despite its ubiquitous and powerful role, the signal contained in an aligned fibril network that induces contact guidance remains unknown. The entire mechanism of contact guidance entails many events beyond signal sensing, for example, mechanotransduction pathways and spatial regulation of cell pseudopods. However, before the entire mechanism of contact guidance in response to aligned fibril networks can be understood, the signal(s) contained in aligned fibrils that induce contact guidance must be identified. Thus, in this study, we isolated anisotropic mechanical resistance as a variable, for fixed anisotropy of adhesion and porosity. If contact guidance is shown to depend on varied anisotropic mechanical resistance, for fixed anisotropy of adhesion and porosity, anisotropic mechanical resistance is established as a sufficient signal (not necessarily the only signal or the dominant signal).

By combining key technologies—magnetic alignment of fibrin gels during fibrillogenesis, active microrheology (AMR) for local network mechanical resistance measurement, cell-compatible cross-linking of fibrin via dityrosine formation, and adhesion blocking antibodies—and ascertaining the effects of cross-linking on fibrin network mechanical resistance anisotropy, fibrin network microstructure, and fibroblast adhesion to fibrin, we established isolation of mechanical resistance anisotropy as the sole variable when cross-linking an aligned fibrin gel. In addition to quantifying variation in mechanical resistance anisotropy with cross-linking using AMR, absence of network microstructure changes was concluded from morphometric analysis of 3D reconstructed confocal reflectance images, and absence of changes in cell adhesion to the fibrin gel was concluded from a centrifugation assay. Altered contact guidance response in the cross-linked aligned gels was ascertained from the cell anisotropy index (AI) based on the tensor of cell orientation, defined by the orientation of the long axis for each cell. Finally, the same contact guidance experiment performed with cells pretreated with a combination of antibodies against $\alpha_v\beta_3$ integrin and β_1 integrin, which are shown to substantially inhibit cell adhesion in these gels based on the centrifugation assay, was performed to assess whether adhesion is contributing to the contact guidance response when mechanical resistance anisotropy is an operative signal; the same contact guidance experiment was also performed in the presence of a fibrinolysis inhibitor to assess whether fibrinolysis must be considered to interpret the findings. The data show that fibroblasts exhibit contact guidance in a network of aligned fibrin fibrils via sensing anisotropy of mechanical resistance, modulated by integrin-mediated adhesion.

Results

Magnetic Alignment and Photo–Cross-Linking Create Uniformly Aligned, Stiffened Fibrin Gel. As a first step toward isolating mechanical resistance anisotropy as a signal for contact guidance, a uniformly aligned guidance field was created by exposure of a fibrin-forming solution to a high-strength magnetic field (9.4 T) during fibrillogenesis to completion. The alignment of the fibrils is maintained upon removal of the gel from the magnet due to the highly entangled network microstructure. Subsequently, the stiffness of these aligned gels was modulated via ruthenium-based photo–cross-linking (simply "cross-linking" hereafter), which induces dityrosine bond formation, presumably both within and between the fibrils. Fig. 2 *A* and *B* shows that fibrin fibrils can be magnetically aligned, and the strength of alignment is not affected by the cross-linking based on polarimetry. Also note the alignment field is highly uniform across a gel within the contact guidance chamber (Fig. 2*A*), so that when cells are entrapped to perform the contact guidance assay, their orientation responses throughout the gel can be pooled. The large retardation values obtained for aligned gels in comparison to control gels that were not exposed to the magnetic field further indicate the strength of fibril alignment (Fig. 2*B*). No difference in retardation existed between the aligned groups with and without cross-linking ($P = 0.775$). Visual inspection of fibril morphology and orientation via confocal reflectance imaging further confirmed the overall fibril alignment along the direction of the magnetic field with no apparent difference between the aligned gels that were cross-linked and noncross-linked (Fig. 2*C*). Also, control gels exhibited randomly oriented fibrils, consistent with a small retardation and a near-isotropic state. Next, to determine whether there is any effect on the bulk mechanical behavior of the fibrin gel upon cross-linking as would be expected, the compressive stress–strain response of control (nonaligned) gels was assessed (Fig. 2*D*).

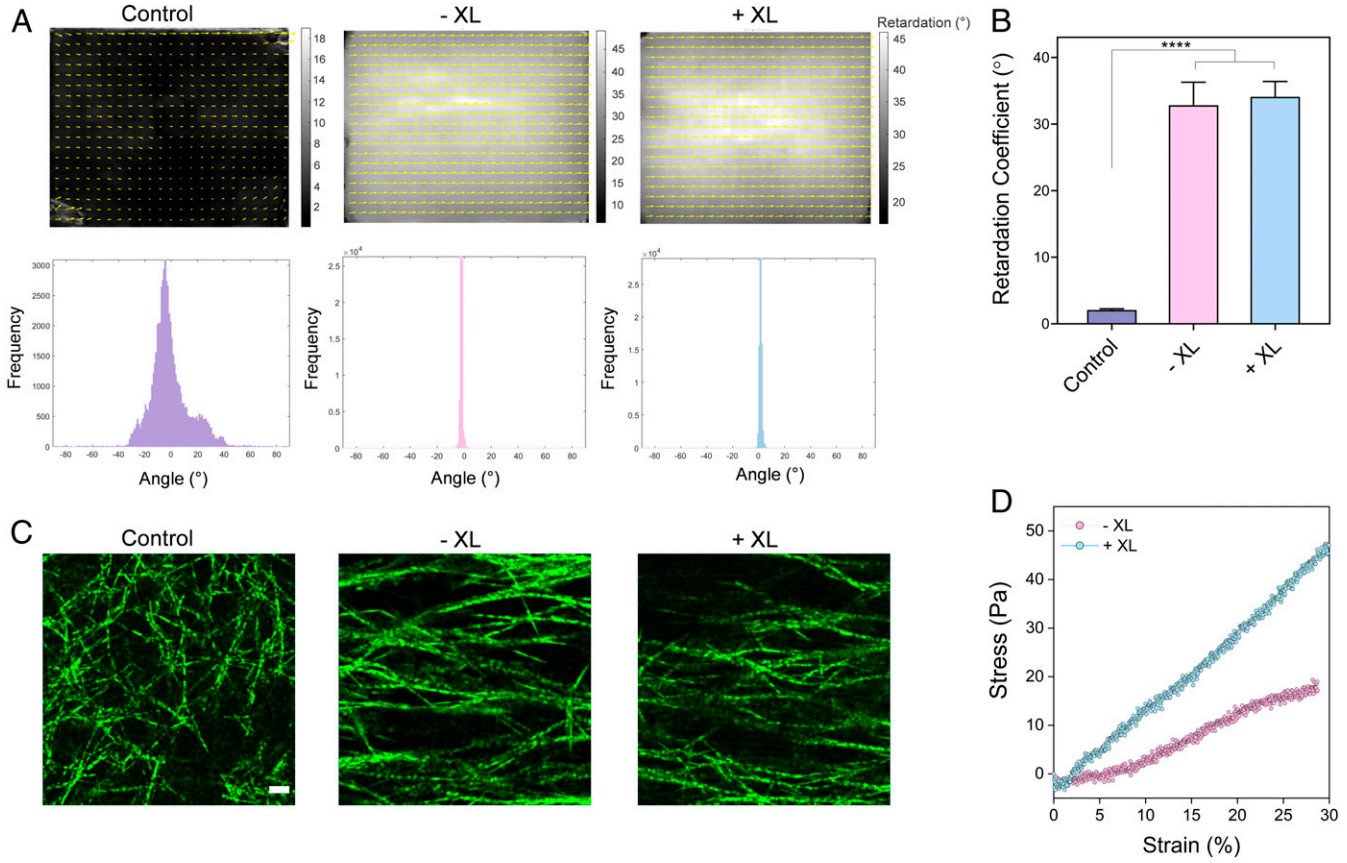

Fig. 2. Generation of magnetically aligned and cross-linked fibrin gels for contact guidance assessment. (*A*) Comparison of polarimetry images of magnetically aligned fibrin gels formed in contact guidance chambers that were either cross-linked or not cross-linked, as indicated. Noncross-linked, nonaligned fibrin gels served as the control. Yellow segments indicate the local average extinction angle (alignment direction) and retardation (strength of alignment), and the background gray level indicates the retardation at each pixel (black = minimum alignment, white = maximum alignment); note the smaller gray level range for the isotropic gel. Associated frequency distribution for local extinction angle reflecting the underlying fibril orientation distribution is shown under each map and is very similar for aligned gels with or without cross-linking. (*B*) The mean retardation coefficient is no different with or without cross-linking. Data are presented as mean ± SD ****$P < 0.0001$ by one-way ANOVA. $n = 3$ guidance chambers for control; $n = 4$ guidance chambers for ±XL groups. (*C*) Confocal reflectance images showing the fibril network microstructure for isotropic and magnetically aligned fibrin gels with or without cross-linking. (Scale bar: 1 μm.) (*D*) Comparison of stress–strain curves of noncross-linked and cross-linked isotropic fibrin gels, obtained from unconfined, uniaxial compression test using a rheometer.

The stress–strain curve and the associated compressive modulus (slope) for cross-linked gels appeared substantially different from the noncross-linked gels prepared at the same time ($P < 0.0001$). Taken together, these results demonstrate our ability to cross-link aligned fibrin gel without any visual change in fibril morphology and network microstructure and to stiffen fibrin gel, at least the bulk compressive stiffness, via the cross-linking.

Contact Guidance of Fibroblasts Is Increased for Aligned Fibrin that Is Cross-Linked. To ascertain whether cross-linking the aligned fibrin gels altered fibroblast contact guidance, cells entrapped in control gels and fibrin gels aligned in a 9.4 T field with or without subsequent cross-linking were visualized under fluorescence microscope after 6 h of culture. Fibroblasts were largely elongated, and their alignment was pronounced in the aligned gels whereas cells were less elongated and appeared randomly oriented in control (isotropic) gels (Fig. 3*A*). Importantly, the fibroblasts in aligned+cross-linked gels exhibited a narrower orientation distribution, with 67% cells oriented within ±10° of the mean alignment direction, as opposed to 48% in aligned gels that were not cross-linked, as seen in the pooled data for three independent experiments in Fig. 3*B*. Consequently, a greater cell AI was recorded in aligned+cross-linked gels (18% increase, $P = 0.0217$, Fig. 3*C*), indicating a role of cross-linking in eliciting a stronger contact guidance response. Orientation distributions and AI values for the three experiments are presented in *SI Appendix*, Fig. S1.

Cross-Linking Increases Local Mechanical Resistance Anisotropy of Aligned Fibrin. AMR measurements were conducted to assess the effect of fibril alignment and cross-linking on local anisotropy in mechanical properties of the fibrin gels prepared for the contact guidance measurements (Fig. 4). Complex shear modulus (G^*) of the fibril network was measured at the maximum depth into the sample, ~35 μm above the bottom cover glass into the ~2 mm thick gel, in orthogonal X and Y directions. The Y direction corresponds to the axis of fibril alignment in aligned gels. Complete AMR results for elastic (G') and viscous (G'') components of the shear modulus are presented in *SI Appendix*, Fig. S2 *A* and *B* and Table S1. For a set of beads, calculation of G'' yields some negative values, particularly for the cross-linked samples. The X and Y Fourier components (X^* and Y^*) have magnitudes exceeding the mean magnitude of noise at 50 Hz (*SI Appendix*, Fig. S3 and Table S2), showing that negative G'' values are not an artifact of signal detection limits. Importantly, G' and G'' are derived from Fourier components of bead displacements and a linear model of viscoelasticity (16, 17). Consequently, negative

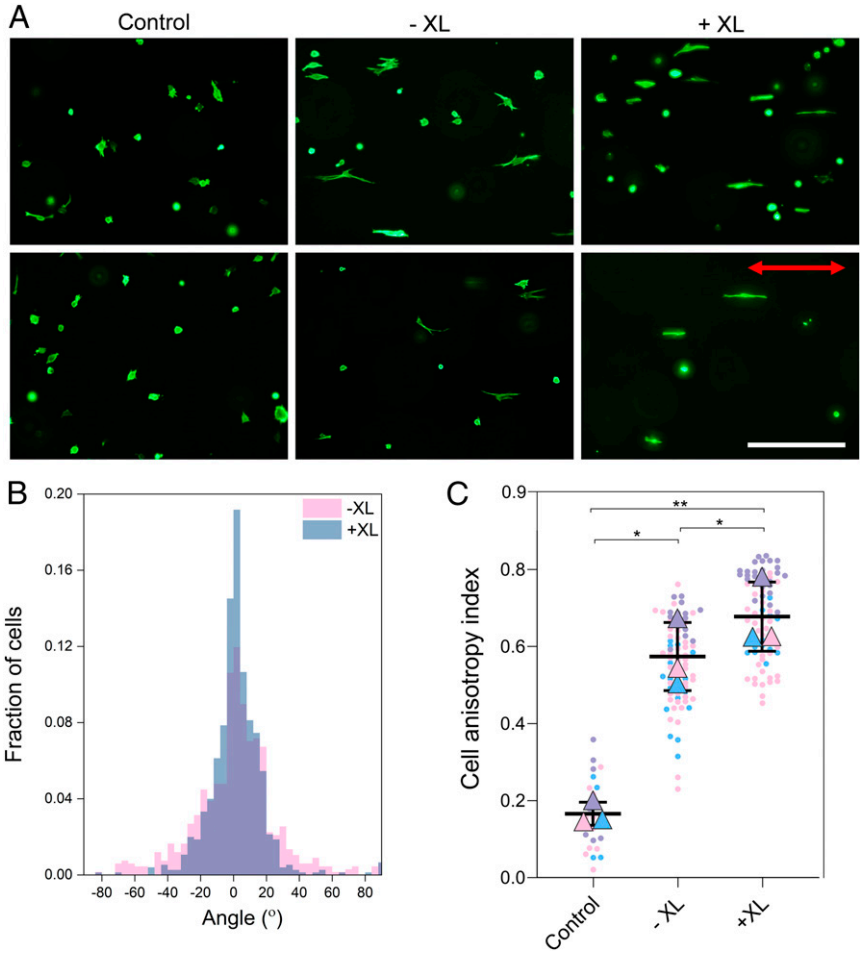

Fig. 3. Modulation of fibroblast contact guidance by cross-linking. (*A*) Representative fluorescence images of cells in control (nonaligned, noncross-linked) gels, aligned noncross-linked (−XL), and aligned cross-linked (+XL) gels. Cells entrapped in the gels were stained for F-actin (phalloidin) at 6 h after seeding and then imaged. The direction of fibril alignment is indicated by the red arrow. (Scale bar: 200 μm.) (*B*) Angular histogram showing cell orientation distribution in aligned noncross-linked versus aligned+cross-linked gels. Increased frequency of alignment at 0° can be noted in aligned+cross-linked gels, suggesting preferential cell orientation along the direction of fibril alignment. Analysis by Kolmogorov–Smirnov test indicates a statistically significant difference between the two angular distributions ($P < 0.001$). $n = 669$ cells for aligned−cross-linked group, and $n = 751$ cells for aligned+cross-linked group, pooled from three independent experiments. Purple shading denotes the overlap distribution of cell orientation values between aligned−cross-linked and aligned+cross-linked groups. (*C*) Quantification of cell AI showing stronger guidance exhibited by cells in aligned+cross-linked gels. Data are presented as scatter plot showing the distribution of data pooled from three independent experiments that is color coded based on the experiment. Corresponding mean calculated from each experimental repeat is denoted in triangle symbol, and the error bars represent mean ± SD calculated from these three means. $*P < 0.05$, $**P < 0.01$, one-way ANOVA with Tukey's multiple comparisons, $n = 3$.

G' and *G"* measurements indicate nonlinear viscoelastic rheology of the network, which is especially induced by the cross-linking.

In order to quantify mechanical properties of the fibrin gels without making the assumption of linearity of network viscoelasticity, we focused on the signals of bead oscillations at 50 Hz in the Fourier space (Fig. 4*A*). Magnitudes of X^* and Y^* are related to compliance of the system, and hence, in order to describe the mechanical resistance of the fibril network to bead oscillations, R, we compared the inverse of magnitudes $|X^*|^{-1} = R_X$ and $|Y^*|^{-1} = R_Y$ at the drive frequency. Due to small discrepancy (up to 11%) in optical trap stiffness along the X and Y directions, we scale R_Y by the ratio of trap stiffnesses k_{trapY}/k_{trapX}. Median and confidence interval (CI) for each distribution were estimated by bootstrapping with replacement of 100 samples and presented as median: [CI_{low}, CI_{high}]. The resulting estimated median and 95% CIs are listed below and in *SI Appendix*, Table S3*A*. The results in *SI Appendix*, Table S3*B* describe population medians and interquartile intervals of the original data (no bootstrapping), and these data were used for statistical testing, which are summarized in *SI Appendix*, Table S3 *C–E*.

Gels that were not magnetically aligned are essentially isotropic in R, while magnetically aligned gels are anisotropic in R, with mechanical resistance higher in the direction of fibril alignment ($R_Y > R_X$; Fig. 4*B*). As compared to isotropic gels, aligned gels also exhibit a larger ratio R_Y/R_X and a larger difference $R_Y - R_X$ (Fig. 4 *C* and *D*).

Cross-linking increased R in both isotropic and aligned gels. In isotropic gels, R_X increased with cross-linking from 2.61: [2.20, 2.95] to 11.61: [10.79, 14.74] × 10^6/μm, and R_Y increased from 2.32: [2.09, 3.02] to 15.94: [13.96, 20.33] × 10^6/μm, consistent with Fig. 2*D*. In aligned gels, R_X increased with cross-linking from 1.72: [1.50, 1.98] to 16.00: [13.69, 16.89] × 10^6/μm, and R_Y increased from 3.28: [3.12, 3.82] to 25.07: [23.39, 27.49] × 10^6/μm (Fig. 4*B*). Importantly, cross-linking of the fibrin gels also increased $R_Y - R_X$ in aligned gels from 1.61: [1.12, 1.94] to 7.08: [5.71, 9.08] × 10^6/μm (Fig. 4*D*). As expected, the ratio of R_Y/R_X is found to be not different between cross-linked and noncross-linked isotropic gels, but,

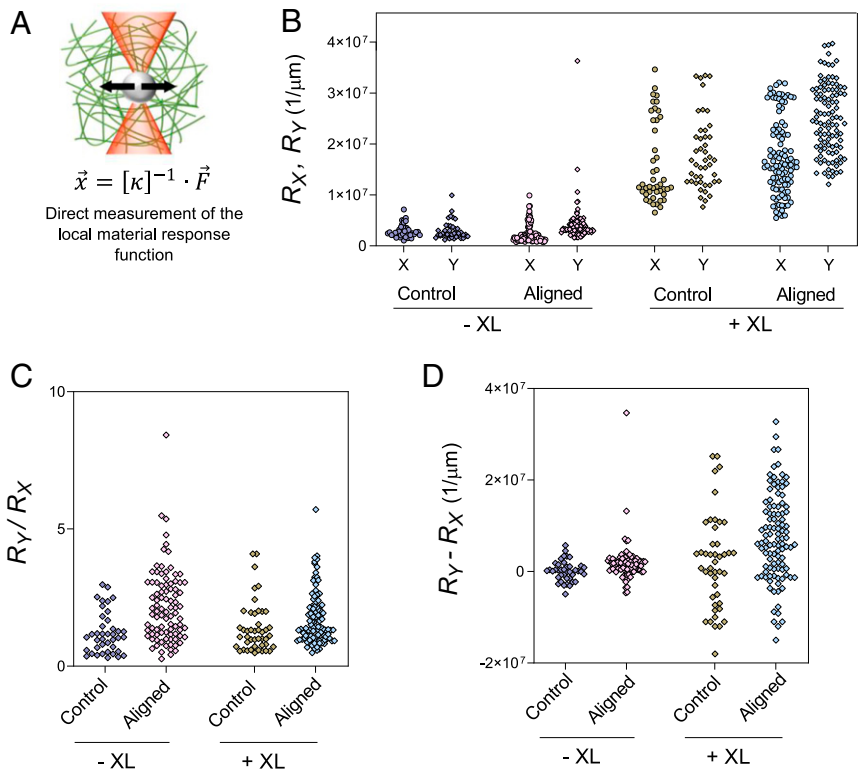

Fig. 4. Local directional mechanical resistance in aligned fibrin gels. (*A*) Graphical representation of optical tweezers AMR. The focused optical tweezers beam (red) is oscillated sinusoidally and exerts oscillatory force on a trapped bead (gray). Fibrin fibrils (green) resist the motion of the bead. Bead displacement and associated shear modulus are calculated from measured laser focus and bead displacement signals. (*B*) The absolute value of the amplitude of the Fourier component of bead displacement at the drive frequency is defined as ($|X^*|$). We further define $|X^*|^{-1} = R_X$ and $|Y^*|^{-1} = R_Y$ with the Y direction corresponding to the axis of fibril alignment. (*C*) Directional mechanical resistance ratio, R_Y/R_X. (*D*) Directional mechanical resistance difference, $R_Y - R_X$. Note in particular the increase in $R_Y - R_X$ after cross-linking (*SI Appendix*, Table S3*E*), which establishes feasibility of testing the mechanical resistance anisotropy hypothesis of contact guidance.

interestingly, it decreased following cross-linking of the aligned gels (Fig. 4*C*). The high variance in R_Y and R_X and occurrences of $R_Y - R_X < 0$ and $R_Y/R_X < 1$ for some measured beads are consistent with the heterogeneity of the fibrin microstructure evident in Fig. 2.

Cross-Linking Does Not Change Fibrin Gel Microstructure. In order to show anisotropic mechanical resistance was isolated as a variable using the cross-linking and conclude it is a sufficient signal for contact guidance, it was necessary to show anisotropy of adhesion and porosity were not changed by cross-linking. As evidence that it did not change anisotropy of porosity, we sought to show it did not change the fibril network microstructure and, therefore, any porosity anisotropy. *SI Appendix*, Fig. S4 *A* and *B* shows a reconstructed network for a single confocal reflectance microscopy (CRM) image for an aligned and cross-linked fibrin gel and three representative morphometric values for samples prepared simultaneously with those used to generate the AMR data presented in Fig. 4. Importantly, a comparison of the gels that were aligned and aligned+cross-linked shows no detectable effect of the cross-linking on the fibrin network microstructure ($P = 0.8037$). Also, there was no difference in fibrin microstructure within a sample at 35 μm or 100 μm above the cover glass where the AMR and contact guidance measurements are made, respectively (*SI Appendix*, Fig. S4*C*). A comparison of values for aligned and nonaligned (isotropic) gels shows the morphometric analysis can detect microstructure differences, specifically the fibril AI (*SI Appendix*, Fig. S4*D*).

Cross-Linking Does Not Change Adhesion of Fibroblasts to Fibrin Gel, Mediated by Integrins. In order to show anisotropic mechanical resistance was isolated as a variable using the cross-linking and conclude it is a sufficient signal for contact guidance, it was also necessary to show anisotropy of adhesion was not changed by cross-linking. As evidence that it did not change anisotropy of adhesion, we also sought to show it did not change the cell adhesion strength and, therefore, any adhesion anisotropy. *SI Appendix*, Fig. S5*A* shows that the fraction of fibroblasts remaining adhered to fibrin gel decreased with increasing detachment (centrifugal) force, as expected, and, importantly, there was no difference in fibroblast adhesion ($P > 0.05$) at any force for samples that were cross-linked and not cross-linked in all three experiments conducted.

In order to subsequently determine the role of varying cell adhesion on contact guidance attributable to sensing of mechanical resistance anisotropy, we also performed integrin-blocking experiments. As a first step, we tested the effect of antibodies against specific integrins for their ability to block adhesion (*SI Appendix*, Fig. S5*B*). As determined from the centrifugation assay, inhibiting $\alpha_v\beta_3$ integrin, which recognizes fibrin, had a minimal effect on cell adhesion, whereas blocking β_1 integrins, including $\alpha_5\beta_1$ that specifically binds to fibronectin associated with fibrin, significantly reduced the percentage of cells bound to ~40% (*SI Appendix*, Fig. S5*C*). However, the greatest decrease occurred using the combination of $\alpha_v\beta_3$ and β_1 integrin-blocking antibodies, resulting in up to 80% reduction in cell adhesion (*SI Appendix*, Fig. S5*C*). The results clearly indicate that a combination of anti-$\alpha_v\beta_3$ and anti-β_1 antibodies is effective in modulating the adhesion

of fibroblasts to fibrin gel. Next, to verify that the treatment with integrin-blocking antibodies does not alter cell spreading, we visualized the morphology of antibody-treated cells entrapped in isotropic fibrin gel after 6 h in culture. Fluorescence images displayed in *SI Appendix*, Fig. S5*D* showed no distinct morphological changes in the antibody-treated group compared to the untreated control. Consistent with the fluorescence images, semiquantitative analysis of cell circularity further confirmed that the function-blocking integrin antibodies had no effect on 3D cell spreading (*SI Appendix*, Fig. S5*E*).

Function-Blocking Integrin-Specific Antibodies Reduce Cell Contact Guidance. Next, we examined the role of the global (or baseline) level of cell adhesion in the contact guidance response of fibroblasts entrapped in aligned fibrin gel, for which mechanical resistance anisotropy can be concluded as operative. The same contact guidance experimental protocol was repeated with the same pretreatment of the fibroblasts with blocking antibodies against $\alpha_v\beta_3$ and β_1 integrins or a combination of both. After 6 h of culture in the magnetically aligned fibrin gel, a moderate decrease in the guidance response was apparent in response to adhesion blocking irrespective of the blocking antibodies used (Fig. 5*A*). The morphology and pseudopodial elongation of the cells pretreated with the combination of the anti-$\alpha_v\beta_3$ and anti-β_1 integrin antibodies did not seem to differ from the untreated cells, as can be seen from the single-cell fluorescent images in Fig. 5*B*. The greatest decrease occurred in cells pretreated with a combination of the anti-$\alpha_v\beta_3$ and anti-β_1 integrin antibodies based on quantification of the cell AI, which revealed a 25% decrease when treated with this antibody combination (Fig. 5*C*). It can also be noted that the fibrin gel retardation coefficient, a measure of fibrin alignment, showed no apparent difference, indicating that the degree of fibril alignment inducing contact guidance was the same across all the treatment groups (Fig. 5*D*). All these data collectively suggest a role of integrin-mediated adhesion in governing the guidance response in conjunction with mechanical resistance anisotropy.

Irrespective of the mechanism, it is generally accepted that pseudopod activity leads to sensing and subsequent cell orientation along the direction of fibril alignment. Hence, we analyzed the directional distribution and length of pseudopods. Consistent with Fig. 5*A*, cells exhibited pseudopods that were predominantly oriented along the direction of the aligned fibrils, on average six times more frequent in the fibril alignment direction than the

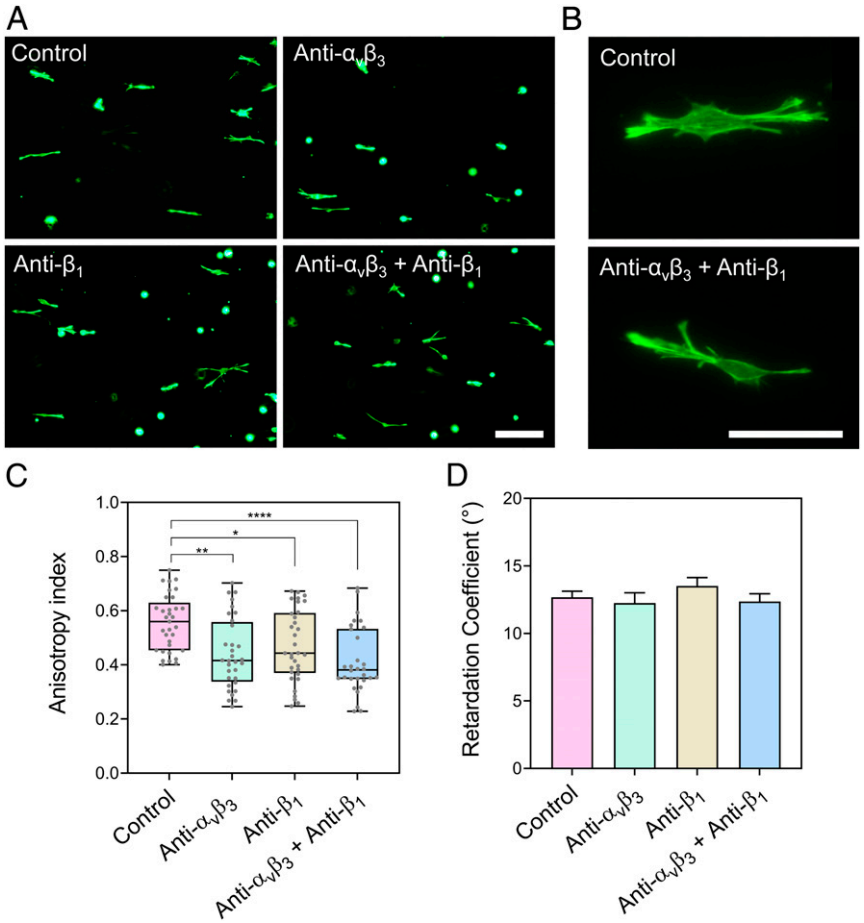

Fig. 5. Modulation of fibroblast contact guidance by integrin-blocking antibodies. (*A*) Representative fluorescence images of fibroblasts entrapped within aligned fibrin gels indicating a decrease in contact guidance in response to blocking antibody treatment. (Scale bar: 200 μm.) (*B*) High power images of representative cells in the control and antibody combination groups for comparison of morphology. (Scale bar: 200 μm.) (*C*) Quantification of the cell AI, comparing the fibroblast guidance response upon treatment using anti-$\alpha_v\beta_3$ antibody or anti-β_1 antibody or a combination of both. The cell orientation in the aligned fibril direction was decreased upon combined blocking of $\alpha_v\beta_3$ and β_1 integrins. ($n = 6$ per condition from two independent experiments; at least five random 10× images of each sample were used in the analysis. $^*P < 0.05$, $^{**}P < 0.001$, $^{****}P < 0.001$, one-way ANOVA). Data are presented as median (middle line) with boxes showing 25th to 75th percentile and whiskers showing minimum to maximum values. (*D*) Average retardation coefficient shows no difference in fibril alignment strength among all the groups tested. Data are presented as mean ± SD. $n = 6$ from two independent experiments.

orthogonal direction; interestingly, the combination of $\alpha_v\beta_3$ and β_1 integrin antibodies did not affect pseudopod length and orientation (*SI Appendix*, Fig. S6).

Fibrinolysis Inhibition Does Not Alter Cell Contact Guidance. In parallel with adhesion inhibition, we also tested the effect of fibrinolysis inhibition on fibroblast spreading in isotropic fibrin gels and contact guidance response in aligned fibrin gels. To explore potential effects, these samples were cultured in medium supplemented with 2 mg/mL ε-aminocaproic acid (ACA), a known fibrinolysis inhibitor. Although there was a 16% reduction of pseudopod length of fibroblasts cultured in nonaligned (isotropic) fibrin gels with ACA supplementation, there was no effect on contact guidance response in aligned gels with the same ACA treatment (*SI Appendix*, Fig. S7).

Discussion

Taken together, these data indicate that fibroblasts can sense aligned fibrils via mechanical resistance anisotropy of the fibril network. The data presented indicate that the cross-linking used does not affect fibroblast adhesion to fibrin or fibrin gel microstructure. Furthermore, Fig. 4 shows increased mechanical resistance anisotropy ($R_Y - R_X$) with cross-linking, and Fig. 3 shows stronger contact guidance (cell AI) with cross-linking. This is a definitive demonstration of a biophysical signal that is being sensed by fibroblasts cultured within aligned fibrils; it is not confounded by simultaneous changes in adhesion and porosity anisotropy. Given the experimental design, the results do not exclude the possibility that the fibroblasts also sense aligned fibrils via adhesion and/or porosity anisotropy as hypothesized by Dunn (15).

However, we also show that modulation of the baseline level of adhesion via function-blocking antibodies can modulate the guidance response when sensing mechanical resistance anisotropy is operative. One interpretation is that adhesion is required to sense the mechanical resistance anisotropy so that modulating the baseline level of adhesion alters the mechanical resistance (and its anisotropy) that is sensed. This most obviously applies if the resistance is sensed by retracting pseudopods adherent to the fibrils via integrins (the types being blocked); this is consistent with the ability of the fibroblasts entrapped in the aligned fibrin to spread with normal morphology when pretreated with integrin antibodies that nearly eliminate adhesion to a fibrin gel surface (i.e., pseudopod extension is adhesion independent, and so, the reduction of contact guidance with the antibody treatment implicates mechanical resistance during retraction of adherent pseudopods). Another interpretation is that the blocking antibodies are altering adhesion anisotropy (numbers of bound integrins on pseudopods projected along and against the direction of fibril alignment), which is not measurable at present. Thus, while sensing mechanical resistance anisotropy is sufficient to induce contact guidance, it may not be dominant, or even necessary, for contact guidance, and it is modulated by the baseline level of adhesion due to intrinsic coupling of pseudopod adhesion and network fibrils in sensing mechanical resistance.

Moreover, the AMR data indicate the cells sense mechanical resistance anisotropy as a directional difference ($R_Y - R_X$), not a directional ratio (R_Y/R_X), that is, the cells are performing subtraction rather than division, at least for the case of aligned gels with increased mechanical resistance anisotropy resulting from the cross-linking. Consideration of a directional ratio was motivated by the classic finding that neutrophils sense the relative concentration difference of the chemotactic peptide fMLP across the cell dimension (ΔC/C) and not the absolute difference (ΔC) owing to optimal gradient sensing when $C \sim K_D$ where K_D is the equilibrium dissociation constant for binding of the chemotactic factor to the cell surface receptor (18). The analogies of ΔC: $R_Y - R_X$ and ΔC/C: $R_Y/R_X - 1$ are noted. Exactly how this finding of directional difference sensing of mechanical resistance is reconciled with biophysical theories of 3D cell motility and migration (19) remains to be determined, but previous studies have shown that the actomyosin system is necessary for fibroblast migration in a 3D matrix (20) such as the fibrin gel used in this study. Thus, the possibility that cells sense mechanical resistance anisotropy when traction develops upon pseudopod retraction as a directional difference—the traction resultant in a "tug-of-war"—as Dunn originally hypothesized (Fig. 1) seems entirely reasonable. Moreover, R_Y/R_X decreased with cross-linking, whereas $R_Y - R_X$ increased and contact guidance was stronger with cross-linking, consistent with sensing a directional difference of mechanical resistance.

Recent work by our group uses this multi-axis AMR system to measure collagen network stiffness heterogeneity and anisotropy surrounding dermal fibroblast and MDA-MB-231 malignant mammary epithelial cells cultured within collagen gel (21). This study used two-axis AMR for the measurement of material property anisotropy in the fibrillar network of a fibrin gel. In related experiments to those presented here, albeit at a lower fibrin concentration, we found that AMR of these 2-μm-diameter beads induced in-phase fiber fluctuations at the drive frequency for a subset of fibrils spanning at least several pore structures away from the bead (22). In other words, fibrils under tension were detected along "force highways" well beyond the pore of the bead. We further found that changing the axis of bead oscillation resulted in a different set of fibrils carrying the tension. Cells exert as much as a 100-fold larger force magnitude than a laser-trapped bead. Thus, we can extrapolate that a contracting pseudopod will engage the local network beyond its attachment point and that a different set of fibrils are engaged depending on pseudopod orientation. It is understandable how these processes can result in the detection of mechanical resistance anisotropy by the cell.

Other hypotheses subsequent to those proposed by Dunn could be proposed, for example, anisotropic proteolysis resulting from diffusion anisotropy of secreted proteases. All these derive from anisotropy of a biophysical signal intrinsic to an aligned fibril network. They are all distinct from anisotropies of cell responses to aligned fibrils, for example, cell traction anisotropy, which is suggested by the finding that collagen fibrils in tension are more resistant to proteolysis (23). However, our results showing no effect on contact guidance with fibrinolysis inhibition indicate that diffusion anisotropy of plasminogen activators is not the biophysical signal intrinsic to an aligned network of fibrin fibrils for fibroblasts.

Interpretation of the AMR results is complicated by the occurrence of nonlinear viscoelastic behavior in the cross-linked gels, notably fitted values of $G'' < 0$. However, linear behavior (G' and $G'' > 0$) occurred for almost all beads for the noncross-linked gels, both isotropic and aligned, allowing for interpretation of the relative contributions of elastic and viscous properties of the network response. In this case, we observed $G''/G' \sim 0.1$, in agreement with our prior studies of noncross-linked fibrin gels (16). For a linear viscoelastic fluid, which describes the fibril network of a fibrin gel at low strains and strain rates, in oscillation with frequency ω, the friction anisotropy experienced by an extending/retracting pseudopod with network strain amplitude γ_0 and strain rate $\sim \omega\gamma_0$ in terms of $G''_Y - G''_X$ would thus only be ~10% of the stiffness anisotropy $G'_Y - G'_X$. Notwithstanding the possibility of a stronger signal amplification of friction anisotropy, the data suggest stiffness anisotropy would be dominant over friction anisotropy. The occurrences of fits with $G'' < 0$ indicates that the response of the system cannot be interpreted as being linear in the applied force. The presence of these nonlinear rheological effects of the intra- and interfibrillar cross-linking despite no detectable change in microstructure is consistent with

nonlinear response of nematically aligned fiber networks (24) and will be a basis for further investigation.

The substantially higher AI value for the fibroblasts relative to the fibrils is striking, suggesting the cells are highly sensitive to the signal presented by the aligned fibrils. A comparison can be made to our previous study of fibroblast alignment in response to collagen fibril alignment when applying an unconfined compression to a collagen gel with entrapped fibroblasts (25). In that study, a functional relationship between the cell and fibril orientation tensors determined by a contact guidance sensitivity parameter, κ defined in a continuum theory of cell–gel mechanical behavior was tested. $\kappa = 1$ indicates the cells align with the same strength as the fibrils, and κ of increasing value above 1 indicates increasing contact guidance sensitivity for a given fibril alignment. Those data were fitted to estimate $\kappa = 5.1$. Estimation of κ using the data presented here for fibroblasts in magnetically aligned fibrin gel yields $\kappa = 5.7$ (*Appendix*), a remarkable agreement indicating that the network microstructure is dominant over the molecular composition information contained therein. Calculating a sensitivity for the dependence of fibroblast contact guidance on mechanical resistance anisotropy associated with the aligned fibrils would require measuring AI on gels of varied $R_Y - R_X$, which could be generated by varied cross-linking conditions that do not change the cell adhesion or network microstructure.

The origin of the increase of $R_Y - R_X$ with cross-linking is unknown, but not necessary knowledge for the purpose of this study. The relatively high content of tyrosine in fibrinogen and complex topology of the fibrin network, which is associated with fibronectin from the serum or produced by the fibroblasts, makes both intra- and interfibrillar cross-linking likely. Nonetheless, it will be of interest to ascertain whether microstructural models (26, 27) can predict this behavior and provide insight into the origin for this rheological behavior.

Once the dominant signal for contact guidance intrinsic to aligned fibrils is identified, future studies can then relate the signal transduction/motility response pathways (28–30) to this signal, including 1) the deposition of aligned collagen by fibroblasts cultured over long periods in aligned fibrin gel that is central to our engineering of heart valves (9, 31) and arteries (8, 32) possessing physiological anisotropic stiffness and 2) the alignment of cardiomyocytes and forming microvessels in our engineered myocardium (33, 34) and microvascular networks (35, 36), respectively, that can confer functional efficiency. Clearly it will be of interest to compare other cell types to these findings for fibroblasts and to compare single cells and multicellular assemblies, such as endothelial cells and self-assembling endothelial tubules (microvessels) in this system.

Using aligned fibrin gel for this study is not to say contact guidance in aligned collagen gel is not important, as it has obvious relevance to connective tissue homeostasis. In fact, the same general framework used here can be attempted in the collagen system since there are multiple methods to cross-link collagen, but whether any one of them isolates mechanical resistance anisotropy would have to be ascertained. A recent study using mechanically aligned collagen gel reported reduced contact guidance of MDA-MB-231 (mesenchymal) cancer cells when the collagen was cross-linked via glycation (37), which is known to stiffen collagen gel aligned via cell compaction (38), is such an example. The aforementioned agreement in the estimates of κ suggest that the signal that dominates contact guidance in an aligned fibrin gel is the same as for aligned collagen gel. We have shown fibrin gel is superior to collagen gel for tissue engineering of connective tissues (39), which led to our use of fibrin as a sacrificial scaffold in our cardiovascular engineering applications summarized above and explains why we chose it for this study. Contact guidance in aligned fibrin likely plays a role in many processes related to wound repair, healing, and regeneration that involve a blood clot, which is essentially a fibrin gel as used in this study containing blood cells. Tension within these clots can lead to their alignment and induction of contact guidance, a hallmark of peripheral nerve regeneration (40).

There are potential limitations to our experimentation leading to the conclusion that fibroblasts can sense anisotropic mechanical resistance intrinsic to aligned fibrin fibrils. While the size of a typical pseudopod is larger than 2-μm dimension and clearly leads to the interaction with multiple fibrils simultaneously (i.e., the fibril network), it is not clear what bead diameter used in AMR best emulates the pseudopod size and the force it exerts on the local network. Other microbead diameters besides 2 μm could be used to establish stiffness anisotropy over a range of pseudopod-network interaction length scales. Diameters of 4.7 and 10 μm have been shown to faithfully probe fibrin network viscoelasticity with AMR, that is, exhibit constrained Brownian motion in 2.5 to 10 mg/mL fibrin gels (41). There are inherent limitations to using the CRM images to demonstrate an absence of microstructure changes from the cross-linking, specifically spatial resolution limitation and 3D reconstruction accuracy. However, alternatives present their own peculiar limitations, for example, the preparation artifacts and limited spatial domain with electron microscopy. Concerning limitations related to the cell adhesion studies, there are various methods to assess cell adhesion, but we are not aware of any method that can quantify adhesion force for cells embedded within a fibrin gel (as measured in our contact guidance experiments, which were intentionally 3D to maximize physiological and tissue engineering relevance). Conversely, there are many methods to quantify adhesion force of cells spread on a fibrin gel (42) and indirectly assess cell adhesion, such as through focal adhesion formation (43). The relatively short 6-h duration of the contact guidance assay was intended to maximize cell adhesion via integrin binding versus focal adhesions, consistent with the efficacy of the blocking antibodies directed against integrin-binding domains on fibrin and fibrin-associated fibronectin. While we are confident that the centrifugation assay used can measure changes in cell adhesion force, it has limited resolution like any measurement, and cell adhesion force may not be relevant to pseudopod–fibril adhesive interactions, for example, as compared to sub-failure strain of bound integrins. However, findings reported for a very similar system of primary fibroblasts seeded on fibrin gel and (separately) entrapped in fibrin gel showed that the cell–matrix adhesion structure area per cell and structure morphology based on immunostaining of β_1 integrins via a label-activating antibody were the same for fibroblasts entrapped in fibrin gel ("3D") as seeded on a fibrin gel layer ("2D") (44), the latter being analogous to the configuration used for our centrifugation assay. Thus, it is reasonable to expect that the integrin blocking by the antibodies we used and demonstrated to reduce cell adhesion with the centrifugation assay would be similarly efficacious in reducing adhesion for the cells we entrapped in fibrin for the guidance assay. The short duration, along with a very low cell concentration, was also used to maximize the likelihood that our measurement of contact guidance was for isolated cells responding to the initial contact guidance field of magnetically aligned fibrin as they initially spread; the consequences of local fibril restructuring by the cells and potential guidance field amplification occurring over time were minimized. Even though this amplification can occur by the pseudopodial activity of single cells (e.g., figure 7 of ref. 11), they still respond to the macroscopic alignment field in a graded fashion (i.e., the strength of fibroblast contact guidance response increases with strength of fibril alignment in collagen gels aligned with magnetic fields of increasing strength).

Despite these potential limitations, the data collectively support the hypothesis of Dunn that fibroblasts can exhibit contact

guidance in aligned fibrils via sensing of mechanical resistance anisotropy of the aligned fibril network, a definitive test of this hypothesis. Whether or not this is the dominant signal among other potential anisotropies presented by the network, such as adhesion or porosity, will require further experimentation that can also isolate these variables.

Materials and Methods

Cell Culture. Human dermal fibroblasts (Lonza) were maintained in a 50/50 mixture of Dulbecco's Modified Eagle's Medium (DMEM) and Ham's F-12 cell culture medium (DMEM/F12, Cellgro) supplemented with 15% fetal bovine serum (FBS, Thermo Fisher Scientific), 100 U/mL penicillin, and 100 U/mL streptomycin (Gibco) at 37 °C. Cells expanded to passage 5 to 7 were used as described.

Fibrin Gel Formation. Fibrin gels were formed by adding bovine thrombin (Sigma) reconstituted in 1× Dulbecco's phosphate-buffered saline with calcium and magnesium ($DPBS^{++}$; Gibco) to a suspension of cells in bovine fibrinogen (Sigma) solution similarly reconstituted in 1× $DPBS^{++}$. For acellular gels, no cells were premixed into the fibrinogen solution. The final component concentrations of the cell suspension were as follows: 4 mg/mL fibrinogen, 0.2 U/mL thrombin (Sigma), and 20,000 cells/mL. The gel-forming cell suspension was maintained on ice, mixed gently, and pipetted into a rectangular insert (10 mm × 12 mm × 2 mm) made of gray resin (PlasGRAY V2, Asiga), firmly adhered to a 35-mm glass bottomed culture dish (FluoroDish, World Precision Instruments) as described below according to the experiment. Subsequently after gelation for 30 min at room temperature, cell-containing samples were cultured in DMEM/F12 medium supplemented with 15% FBS (HyClone), 100 U/mL penicillin, and 100 μg/mL streptomycin (Gibco) in the incubator at 37 °C for the duration of the experiment. Acellular samples were maintained in 1× PBS (Gibco).

Magnetic Alignment. Immediately after pipetting the gel-forming solution/cell suspension into the rectangular insert, the sample was placed in the bore of a horizontal bore electromagnet for 30 min while undergoing fibrillogenesis. The field strength in all experiments was 9.4 T. Fibrin fibril alignment in the direction of the magnetic field occurs due to the positive diamagnetic anisotropy of growing fibrin fibrils, and the alignment becomes set due to ensuing entanglements of the fibrin fibrils so that it is preserved after removing the container from the magnet (45, 46).

Cross-Linking. As previously reported (47, 48), ruthenium trisbipyridyl chloride $[Ru(II)(bpy)_3]^{2+}$ solution (henceforth identified as Ru for simplicity) was made at 10× (20 mM) concentration by dissolving it in distilled H_2O. Sodium persulfate (SPS) solution was prepared at 20× (200 mM) concentration by dissolving in distilled H_2O. Solutions were sterile filtered with a 2-μm filter (Millipore). Solutions were protected from light until used and made fresh for each cross-linking experiment. Prior to cross-linking, the solutions were diluted in sterile DPBS, and the gels were incubated in a mixed solution of Ru and SPS pipetted onto their surface at room temperature for 10 min under gentle shaking. At the end of the incubation, the culture dish containing the gel was placed over a custom-built light-emitting diode array powered at an operating current of 25 mA to emit blue light (wavelength 465 ± 5 nm) at fluence of 3820 Lux for 10 s to initiate the cross-linking reaction. The reagents were removed via repeated immersions of the cross-linked gel in sterile DPBS. Gels with entrapped cells were then cultured in DMEM/F12 medium with the supplements described earlier. Controls were kept in normal culture medium and not exposed to blue light but otherwise subjected to the same culture conditions.

Polarimetric Imaging. Polarimetry was used to assess the sample's retardation pattern and infer fibril alignment (49, 50). In this method, extinction angle and retardation are computed on a pixel-wise basis in the region of interest, assuming the fibrin fibrils are strong linear retarders and dominate the change in polarization state of the transmitted light. Polarimetric images are created by averaging local values to create segments with direction corresponding to the local average extinction angle and length proportional to the local average retardation on a background gray level mapped to the pixel-wise retardation.

Unconfined Compression Testing. The bulk mechanical properties of acellular isotropic fibrin gels with or without cross-linking were measured by unconfined compression test using a rheometer (RSA-G2 Solids Analyzer, TA Instruments) at room temperature. A parallel plate fixture of 8-mm diameter was employed, and the fibrin sample was placed in between the upper and lower plate with a gap of 2.5 mm (sample height). The upper plate was moved vertically at a constant displacement rate of 1.2 μm/s to generate the uniaxial compression, and the test was run until the strain reached 30%. Experiments were performed on at least four samples and representative stress–strain curves are shown subsequently.

AMR. Measurements of fibrin resistance to deformation were conducted in acellular fibrin gels using an optical tweezers AMR system previously described (51) but modified to measure material properties along multiple axes (52), in which bead position is detected from backscattered laser beam illumination. For AMR measurements, fibrin gels were prepared at University of Minnesota using the same reagents as used for the cell related experiments. Gel precursor solutions were supplemented with 2-μm-diameter carboxylated silica beads (Bangs Laboratories) at a final bead concentration of 0.8 mg/mL. Gels were prepared, optionally aligned, and optionally cross-linked as described above, and then PBS was added to completely fill the wells of the culture dish, removing all air bubbles. The dish was sealed with parafilm and shipped overnight at room temperature to University of California, Irvine. At the time of measurement, samples were incubated on the microscope stage at 37 °C using a dish incubator and objective lens heater (Warner Instruments). The microscope objective lens is a 60×-oil PlanApo Total Internal Reflection Fluorescence Microscopy (TIRFM) 1.45 NA lens (Olympus) selected to generate a strong optical trap with trap stiffness 30 to 35 pN/μm. During AMR measurements, an oscillatory force is applied to a bead by an oscillating optical trap generated with a 1,064-nm laser (IPG Photonics). Bead position is probed by a focused low-power 785-nm laser diode (Thorlabs). The position of the bead is determined by deflection of the probe beam, which changes linearly with bead displacement. Instantaneous position of the optical trap and the bead are recorded by two quadrant photodiodes (Newport) respectively. Displacement and force vectors are related by the stiffness tensor according to

$$\vec{x} = [\kappa]^{-1} \cdot \vec{F} \qquad [1]$$

where off-diagonal elements are assumed to be equal to 0.

All probed beads were located ~35 μm from the bottom cover glass and at least 3 mm from the sidewalls. Beads were oscillated at 50 Hz first in the X and then in the Y direction with respect to the camera field of view. Y direction corresponded to the axis of fibril alignment in aligned samples. The Fourier transform values X^* and Y^* are calculated from the signals recorded by the quadrant photodiode describing the motion of the bead during bead oscillations in X and Y directions, respectively. $|X^*|^{-1}$ and $|Y^*|^{-1}$ at the oscillation frequency of 50 Hz describe bead motion under optical tweezers forces, which can be interpreted as the fibrin network resistance, R, to an applied force. Thus, $|X^*|^{-1} = R_X$ and $|Y^*|^{-1} = R_Y$. R_Y values are corrected by the ratio of trap stiffnesses during oscillations in X and Y direction. The ratio k_{trapY}/k_{trapX} for the tested samples ranged from 0.98 to 1.11. Elastic (G') and viscous (G'') shear moduli were calculated from optical trap and bead position signals, as described previously (16, 17).

In order to quantify noise present in our system, AMR measurements were conducted when the optical trap was focused 35 μm from the bottom cover glass but was not in proximity of a bead. Mean noise of $|X^*|$ and $|Y^*|$ at 50 Hz was found to be equal to $(2.88 \pm 3.78) \times 10^{-8}$ μm in the X direction and $(2.71 \pm 1.40) \times 10^{-8}$ μm in the Y direction ($n = 7$). Beads for which either $|X^*|$ or $|Y^*|$ were below the mean magnitude of noise measurements at 50 Hz were removed from analysis.

Confocal Reflectance Imaging. The structure of fibrin gels was imaged via CRM using A1RMP multiphoton upright microscopy system (Nikon), using a 25× water-immersion objective lens (Apo LWD, numerical aperture = 1.1, Nikon) and a 488-nm laser line. Z-stacks were collected in Galvano scanner mode with a step size of 1 μm, field of view of 512 × 512, and a lateral resolution of 0.11 μm per pixel.

Contact Guidance Measurement. Magnetically aligned fibrin gels (three to four replicate samples per experiment) containing entrapped fibroblasts were prepared in rectangular inserts attached on a glass-bottom culture dish. The fibrin-forming cell suspension was injected directly into the center of the insert to form a rectangular-shaped gel adherent to the bottom of the

culture dish of size 10 mm × 12 mm and 2 mm thick. Directly after removal from the magnet, the samples were cross-linked and then cultured in DMEM/F12 at 37 °C, 5% CO_2 for 6 h. Cells were then fixed with 4% paraformaldehyde for 30 min, followed by permeabilization using 0.1% Triton X-100 in DPBS for 10 min and blocking using 1.5% bovine serum albumin in DPBS for 30 min. Cells were subsequently stained with Alexa Fluor 488 phalloidin for 30 min, prior to imaging. Z-stack imaging was carried out using an EVOS FL Auto 2 microscope with a step size of 5 μm, at a magnification of either 10× or 20×, with a 470/22 excitation filter and a 510/42 emission filter. All Z-stack images were collected ∼100 μm from the bottom cover glass to ensure no effects of cells settled to and influenced by the cover glass. The images used for analysis were created by combining the stacks of images via rendering using maximum intensity projections. Cell orientation was manually defined by drawing a segment coinciding with the long axis of each cell as projected into the optical plane based on the best fit ellipse determined by ImageJ Particle Analyzer tool for ∼100 cells per sample and then processed using the ImageJ plugin FibrilTool (53) to determine the cell AI for each sample. AI is defined as the difference of the major and minor eigenvalues for the cell orientation tensor and varies from 0 for isotropic orientation to 1 for uniaxial orientation. The steps involved in cell AI measurement using FibrilTool plugin (ImageJ software) are illustrated in *SI Appendix*, Fig. S8. The experiment was conducted three times ($n = 3$).

Cell Adhesion Measurement. A centrifugation assay of cell adhesion (54) was adapted to measure cell adhesion to fibrin gel. Staggered wells in a 96-well culture plate were coated with 50 μL of the fibrin gel-forming solution, sufficient to completely cover the bottom. A total of 5,000 fibroblasts in DMEM complete medium were added to each well and incubated for 24 h. Samples ($n = 4$ to 10 wells per condition) were either cross-linked or not and incubated for 8 h. The wells were then filled with culture medium and were sealed airtight to avoid medium loss and air bubbles. Hoechst 33342 was then added (2 μg/mL). Sealed plates were inverted and subjected to centrifugation for 5 min at 50, 250, and 500 × g for the first two experiments and 50, 200, 400, and 500 × g for experiment three in a swinging bucket rotor with plate holder. Hoechst fluorescence was used to quantify the number of cells in a 10× field in plates restored to upright position after removing all free liquid, following ref. 54. An identical plate not centrifuged was used to quantify standard number of cells per 10× field; this was used to calculate the fraction of cells still adherent. The experiment was conducted three times ($n = 3$).

Cell Adhesion Inhibition. In order to modulate integrin-mediated cell adhesion to fibrin gel, the cells were pretreated with function-blocking monoclonal antibodies against $\alpha_v\beta_3$ integrin (15 μg/mL) (clone LM609, MAB1976Z, Millipore), β_1 integrin (15 μg/mL) (clone P5D2, MAB1959Z, Millipore), or a combination of both in serum-free cell culture medium. After incubation for 30 min, the cells were rinsed in 1× DPBS and seeded onto a 96-well plate precoated with 50 μL of 4 mg/mL fibrin gel. The cells were then allowed to attach for 6 h at 37 °C in 5% CO_2. Subsequently, cell adhesion strength was measured using the centrifugation assay as described above using 500 × g, after labeling with live nuclear stain, Hoechst 33342. Automated cell counting of the fluorescence images (Invitrogen EVOS FL Auto 2 Cell Imaging System) was performed with ImageJ using the "Cell Counter" plugin.

Next, to determine whether the integrin-blocking antibodies affect cell spreading within fibrin gel, the cells identically pretreated with the aforementioned antibodies were entrapped in fibrin gel at a concentration of 10,000 cells/mL and were allowed to spread for 6 h at 37 °C in 5% CO_2. Subsequently, the samples were fixed in 4% paraformaldehyde for 30 min, followed by staining with Alexa 488-phalloidin for F-actin. The morphology of cells was then observed under a fluorescence microscope (Olympus IX70) and cell circularity (defined as $4\pi \times [area]/[perimeter]^2$) was calculated with ImageJ after segmenting the cells. A circularity value of 1 indicates a circular cell, whereas a value decreasing to 0 indicates an increasingly elongated cell.

Fibrinolysis Inhibition. In a separate set of experiments, fibroblasts entrapped in nonaligned and aligned fibrin gels were cultured for 6 h in DMEM/F12 medium supplemented with 2 mg/mL of ACA (Sigma) to inhibit fibrinolysis based on our prior studies (39, 55).

Fibrin Fibril Network Reconstruction and Morphometric Analysis. CRM was used to visualize fibrin fibrils in 4 mg/mL fibrin gels, allowing for network reconstruction and analysis of network morphology (56). Individual image slices of the fibrin networks obtained at 1-μm depth intervals obtained from these confocal stacks were first deconvolved using the Huygens software (Scientific Volume Imaging), then reconstructed using fiber extraction (FIRE) algorithm of Stein et al. (57) From each reconstructed 2D image slice, network morphometric parameters of average fibril length and average connectivity were extracted as previously performed (56). Similar to the cell AI, a fibril AI was computed for each gel based on the major and minor eigenvalues for the associated fibril orientation tensor. AI varies from 0 for isotropic orientation to 1 for uniaxial orientation.

Cell Pseudopod Detection and Quantitation. For the automated image analysis of pseudopods, high-magnification fluorescent images (40×) of single cells were processed in ImageJ to convert the grayscale image into binary image. The locations of the cell centroids, perimeter, and protrusion endpoints were identified using a code in MATLAB (The MathWorks, Inc.) developed by Riching et al. (10) The output generated from the Riching code was then used as an input to determine the start of the pseudopod, length, and orientation using a custom code implemented in LabVIEW (National Instruments). An example of steps involved in pseudopod detection and analysis for a single cell in aligned fibrin gel is illustrated in *SI Appendix*, Fig. S9 *A–K*. The actin-labeled single-cell images (*SI Appendix*, Fig. S9*A*) were preprocessed in imageJ software by converting to binary image, followed by thresholding, and applying the smoothing function (*SI Appendix*, Fig. S9*B*). The algorithm then begins drawing increasing concentric circles about the centroid starting with a small radius, until these circles leave the boundary of the cell on both sides (*SI Appendix*, Fig. S9 *D–K*). When the circle leaves the cell boundary on both sides, then the distance between these points is calculated (*SI Appendix*, Fig. S9*K*). Once the start locations of all pseudopods are determined, the lengths and orientation are subsequently computed.

Statistical Analysis. All the cell and fibrin assay data were analyzed using a two-tailed unpaired t test or the Mann–Whitney U test (for data not normally distributed based on Shapiro–Wilk test) when comparing between two groups and ANOVA when comparing between multiple groups. Cell/pseudopod orientation distributions were compared using Kolmogorov–Smirnov test. Analyses were done by GraphPad Prism 8.4 software. Statistical analysis of AMR data were conducted in MATLAB. Data were found not to be normally distributed, and so nonparametric tests were employed. Mann–Whitney U tests were used for comparison between sample types, and Wilcoxon tests were utilized for comparison of correlated measurements in the X and Y directions within the same sample type. Data are presented as mean ± SD or median ± SD, as indicated in the figure legends. Values of $P < 0.05$ were considered as statistically significant, yielding differences with 95% confidence (*$P < 0.05$, **$P < 0.01$, ***$P < 0.001$, ****$P < 0.0001$).

Appendix Estimation of the contact guidance sensitivity parameter.

In the anisotropic biphasic theory of tissue-equivalent mechanics (7), the contact guidance sensitivity parameter, κ, is defined to functionally relate the cell and fibril orientation tensors, Ω_c and Ω_f:

$$\Omega_c = \frac{\Omega_f^\kappa}{\mathrm{tr}\Omega_f^\kappa} \quad [2]$$

Given the definitions of Ω_c (53) and Ω_f (58) used here, both tensors have traces equal to 1.

Assuming coalignment Ω_c and Ω_f with the chamber axes (off-diagonal elements are zero) for orientation as measured in the 2D plane, Eq. 1 becomes simply

$$\Omega_{c,yy} = \frac{\Omega_{f,yy}^\kappa}{\Omega_{f,yy}^\kappa + \Omega_{f,xx}^\kappa} \quad [3]$$

where y is the direction of alignment and x is the orthogonal direction. With the cell AI = $\Omega_{c,yy} - \Omega_{c,xx} \sim 0.70$ from Fig. 3*C* and $\Omega_{c,yy} + \Omega_{c,xx} = 1 \rightarrow \Omega_{c,yy} \sim 0.85$.

Also, using the FIRE results for fibril AI $\sim 0.16 \rightarrow \Omega_{f,yy} \sim 0.58$ and $\Omega_{f,xx} \sim 0.42$, which yields $\kappa \sim 5.7$ from Eq. **2**.

Data Availability. All study data are included in the article and/or *SI Appendix*. The MATLAB code used for automated detection of pseudopods are available in Zenodo at https://doi.org/10.5281/zenodo.4533281.

ACKNOWLEDGMENTS. We acknowledge the technical assistance of Naomi Ferguson, Taylor Rothermel, Sonja Riemenschneider, David Nedrelow, Emma Wolcott, and the University of Minnesota Center for Magnetic Resonance Research for the use of the facilities and equipment. We are also grateful to Guillermo Marques for helpful assistance in CRM and the University Imaging Center (http://uic.umn.edu/) at UMN for the use of the Nikon A1RMP Confocal

microscope and associated image analysis software (NIS-Elements Confocal, NIS-Elements Confocal Advanced Research). Funding support for this work was provided by NSF/Chemical, Bioengineering, Environmental, and Transport Systems (CBET) Grant 1606008 (to R.T.T.), NIH Grant R01-EB005813, NSF Grant 1763272, University of California Office of the President Grant MRI-17-454791, and NIH Grant R01-HL085339 (to E.L.B.).

1. P. Weiss, "Nervous system (neurogenesis)" in *Analysis of Development*, B. H. Willier, P. A. Weiss, V. Hamburger, Eds. (W.B. Saunders Company, Philadelphia, PA, 1955), pp. 346–401.
2. P. P. Provenzano, D. R. Inman, K. W. Eliceiri, S. M. Trier, P. J. Keely, Contact guidance mediated three-dimensional cell migration is regulated by Rho/ROCK-dependent matrix reorganization. *Biophys. J.* **95**, 5374–5384 (2008).
3. M. Werner, N. A. Kurniawan, C. V. C. Bouten, Cellular geometry sensing at different length scales and its implications for scaffold design. *Materials* **13**, 963 (2020).
4. A. B. C. Buskermolen *et al*., Entropic forces drive cellular contact guidance. *Biophys. J.* **116**, 1994–2008 (2019).
5. I. Tonazzini *et al*., Neuronal contact guidance and YAP signaling on ultra-small nanogratings. *Sci. Rep.* **10**, 3742 (2020).
6. K. Y. Vajanthri, R. K. Sidu, S. Poddar, A. K. Singh, S. K. Mahto, Combined substrate micropatterning and FFT analysis reveals myotube size control and alignment by contact guidance. *Cytoskeleton* **76**, 269–285 (2019).
7. V. H. Barocas, R. T. Tranquillo, An anisotropic biphasic theory of tissue-equivalent mechanics: The interplay among cell traction, fibrillar network deformation, fibril alignment, and cell contact guidance. *J. Biomech. Eng.* **119**, 137–145 (1997).
8. Z. H. Syedain, L. A. Meier, M. T. Lahti, S. L. Johnson, R. T. Tranquillo, Implantation of completely biological engineered grafts following decellularization into the sheep femoral artery. *Tissue Eng. Part A* **20**, 1726–1734 (2014).
9. Z. Syedain *et al*., 6-month aortic valve implantation of an off-the-shelf tissue-engineered valve in sheep. *Biomaterials* **73**, 175–184 (2015).
10. K. M. Riching *et al*., 3D collagen alignment limits protrusions to enhance breast cancer cell persistence. *Biophys. J.* **107**, 2546–2558 (2014).
11. S. Guido, R. T. Tranquillo, A methodology for the systematic and quantitative study of cell contact guidance in oriented collagen gels. Correlation of fibroblast orientation and gel birefringence. *J. Cell Sci.* **105**, 317–331 (1993).
12. R. B. Dickinson, S. Guido, R. T. Tranquillo, Biased cell migration of fibroblasts exhibiting contact guidance in oriented collagen gels. *Ann. Biomed. Eng.* **22**, 342–356 (1994).
13. N. Dubey, P. C. Letourneau, R. T. Tranquillo, Neuronal contact guidance in magnetically aligned fibrin gels: Effect of variation in gel mechano-structural properties. *Biomaterials* **22**, 1065–1075 (2001).
14. P. P. Provenzano, K. W. Eliceiri, D. R. Inman, P. J. Keely, Engineering three-dimensional collagen matrices to provide contact guidance during 3D cell migration. *Curr. Protoc. Cell Biol.* **Chapter 10**, Unit 10.17 (2010).
15. G. A. Dunn, "Contact guidance of cultured tissue cells: A survey of potentially relevant properties of the substratum" in *Cell Behaviour*, R. Bellairs, A. Curtis, G. Dunn, Eds. (Cambridge University Press, Cambridge, 1982), pp. 247–280.
16. M. A. Kotlarchyk *et al*., Concentration independent modulation of local micromechanics in a fibrin gel. *PLoS One* **6**, e20201 (2011).
17. D. Mizuno, D. A. Head, F. C. MacKintosh, C. F. Schmidt, Active and passive microrheology in equilibrium and nonequilibrium systems. *Macromolecules* **41**, 7194–7202 (2008).
18. S. H. Zigmond, Ability of polymorphonuclear leukocytes to orient in gradients of chemotactic factors. *J. Cell Biol.* **75**, 606–616 (1977).
19. K. M. Yamada, M. Sixt, Mechanisms of 3D cell migration. *Nat. Rev. Mol. Cell Biol.* **20**, 738–752 (2019).
20. A. D. Doyle, F. W. Wang, K. Matsumoto, K. M. Yamada, One-dimensional topography underlies three-dimensional fibrillar cell migration. *J. Cell Biol.* **184**, 481–490 (2009).
21. A. Jagiełło, M. Lim, E. Botvinick, Dermal fibroblasts and triple-negative mammary epithelial cancer cells differentially stiffen their local matrix. *APL Bioeng.* **4**, 046105 (2020).
22. E. L. Botvinick, Q. Hu, T. A. Morris, A. Grosberg, A. J. Levine, Actively driven fluctuations in a fibrin network. *Front. Phys.* **8**, 568736 (2021).
23. J. W. Ruberti, N. J. Hallab, Strain-controlled enzymatic cleavage of collagen in loaded matrix. *Biochem. Biophys. Res. Commun.* **336**, 483–489 (2005).
24. L. C. Foucard, J. K. Price, W. S. Klug, A. J. Levine, Cooperative buckling and the nonlinear mechanics of nematic semiflexible networks. *Nonlinearity* **28**, R89–R112 (2015).
25. T. S. Girton, V. H. Barocas, R. T. Tranquillo, Confined compression of a tissue-equivalent: Collagen fibril and cell alignment in response to anisotropic strain. *J. Biomech. Eng.* **124**, 568–575 (2002).
26. V. K. Lai, S. P. Lake, C. R. Frey, R. T. Tranquillo, V. H. Barocas, Mechanical behavior of collagen-fibrin co-gels reflects transition from series to parallel interactions with increasing collagen content. *J. Biomech. Eng.* **134**, 011004 (2012).
27. A. Stein, D. Vader, D. Weitz, L. Sander, The micromechanics of three-dimensional collagen-I gels. *Complexity* **16**, 22–28 (2011).
28. V. K. Raghunathan *et al*., Involvement of YAP, TAZ and HSP90 in contact guidance and intercellular junction formation in corneal epithelial cells. *PLoS One* **9**, e109811 (2014).
29. S. P. Carey *et al*., Local extracellular matrix alignment directs cellular protrusion dynamics and migration through Rac1 and FAK. *Integr. Biol.* **8**, 821–835 (2016).
30. E. D. Tabdanov, V. Puram, A. Zhovmer, P. P. Provenzano, Microtubule-actomyosin mechanical cooperation during contact guidance sensing. *Cell Rep.* **25**, 328–338.e5 (2018).
31. Z. H. Syedain, L. A. Meier, J. M. Reimer, R. T. Tranquillo, Tubular heart valves from decellularized engineered tissue. *Ann. Biomed. Eng.* **41**, 2645–2654 (2013).
32. Z. H. Syedain *et al*., A completely biological "off-the-shelf" arteriovenous graft that recellularizes in baboons. *Sci. Transl. Med.* **9**, eaan4209 (2017).
33. J. S. Wendel, L. Ye, P. Zhang, R. T. Tranquillo, J. J. Zhang, Functional consequences of a tissue-engineered myocardial patch for cardiac repair in a rat infarct model. *Tissue Eng. Part A* **20**, 1325–1335 (2014).
34. J. S. Wendel *et al*., Functional effects of a tissue-engineered cardiac patch from human induced pluripotent stem cell-derived cardiomyocytes in a rat infarct model. *Stem Cells Transl. Med.* **4**, 1324–1332 (2015).
35. K. T. Morin, A. O. Smith, G. E. Davis, R. T. Tranquillo, Aligned human microvessels formed in 3D fibrin gel by constraint of gel contraction. *Microvasc. Res.* **90**, 12–22 (2013).
36. K. T. Morin, J. L. Dries-Devlin, R. T. Tranquillo, Engineered microvessels with strong alignment and high lumen density via cell-induced fibrin gel compaction and interstitial flow. *Tissue Eng. Part A* **20**, 553–565 (2014).
37. J. A. M. Nuhn, A. M. Perez, I. C. Schneider, Contact guidance diversity in rotationally aligned collagen matrices. *Acta Biomater.* **66**, 248–257 (2018).
38. T. S. Girton, T. R. Oegema, R. T. Tranquillo, Exploiting glycation to stiffen and strengthen tissue equivalents for tissue engineering. *J. Biomed. Mater. Res.* **46**, 87–92 (1999).
39. E. D. Grassl, T. R. Oegema, R. T. Tranquillo, Fibrin as an alternative biopolymer to type-I collagen for the fabrication of a media equivalent. *J. Biomed. Mater. Res.* **60**, 607–612 (2002).
40. L. R. Williams, Exogenous fibrin matrix precursors stimulate the temporal progress of nerve regeneration within a silicone chamber. *Neurochem. Res.* **12**, 851–860 (1987).
41. M. A. Kotlarchyk, E. L. Botvinick, A. J. Putnam, Characterization of hydrogel microstructure using laser tweezers particle tracking and confocal reflection imaging. *J. Phys. Condens. Matter* **22**, 194121 (2010).
42. A. A. Khalili, M. R. Ahmad, A review of cell adhesion studies for biomedical and biological applications. *Int. J. Mol. Sci.* **16**, 18149–18184 (2015).
43. D. C. Worth, M. Parsons, Advances in imaging cell-matrix adhesions. *J. Cell Sci.* **123**, 3629–3638 (2010).
44. K. M. Hakkinen, J. S. Harunaga, A. D. Doyle, K. M. Yamada, Direct comparisons of the morphology, migration, cell adhesions, and actin cytoskeleton of fibroblasts in four different three-dimensional extracellular matrices. *Tissue Eng. Part A* **17**, 713–724 (2011).
45. J. Torbet, J. M. Freyssinet, G. Hudry-Clergeon, Oriented fibrin gels formed by polymerization in strong magnetic fields. *Nature* **289**, 91–93 (1981).
46. G. Hudry-Clergeon, J. M. Freyssinet, J. Torbet, J. Marx, Orientation of fibrin in strong magnetic fields. *Ann. N. Y. Acad. Sci.* **408**, 380–387 (1983).
47. Z. H. Syedain, J. Bjork, L. Sando, R. T. Tranquillo, Controlled compaction with ruthenium-catalyzed photochemical cross-linking of fibrin-based engineered connective tissue. *Biomaterials* **30**, 6695–6701 (2009).
48. J. W. Bjork, S. L. Johnson, R. T. Tranquillo, Ruthenium-catalyzed photo cross-linking of fibrin-based engineered tissue. *Biomaterials* **32**, 2479–2488 (2011).
49. T. T. Tower, M. R. Neidert, R. T. Tranquillo, Fiber alignment imaging during mechanical testing of soft tissues. *Ann. Biomed. Eng.* **30**, 1221–1233 (2002).
50. C. S. Jhun, M. C. Evans, V. H. Barocas, R. T. Tranquillo, Planar biaxial mechanical behavior of bioartificial tissues possessing prescribed fiber alignment. *J. Biomech. Eng.* **131**, 081006 (2009).
51. M. Keating, A. Kurup, M. Alvarez-Elizondo, A. J. Levine, E. Botvinick, Spatial distributions of pericellular stiffness in natural extracellular matrices are dependent on cell-mediated proteolysis and contractility. *Acta Biomater.* **57**, 304–312 (2017).
52. A. Jagiełło, M. Lim, E. Botvinick, Dermal fibroblasts and triple-negative mammary epithelial cancer cells differentially stiffen their local matrix. *APL Bioeng.* **4**, 046105 (2020).
53. A. Boudaoud *et al*., FibrilTool, an ImageJ plug-in to quantify fibrillar structures in raw microscopy images. *Nat. Protoc.* **9**, 457–463 (2014).
54. D. R. McClay, G. M. Wessel, R. B. Marchase, Intercellular recognition: Quantitation of initial binding events. *Proc. Natl. Acad. Sci. U.S.A.* **78**, 4975–4979 (1981).
55. K. A. Ahmann, J. S. Weinbaum, S. L. Johnson, R. T. Tranquillo, Fibrin degradation enhances vascular smooth muscle cell proliferation and matrix deposition in fibrin-based tissue constructs fabricated in vitro. *Tissue Eng. Part A* **16**, 3261–3270 (2010).
56. V. K. Lai *et al*., Microstructural and mechanical differences between digested collagen-fibrin co-gels and pure collagen and fibrin gels. *Acta Biomater.* **8**, 4031–4042 (2012).
57. A. M. Stein, D. A. Vader, L. M. Jawerth, D. A. Weitz, L. M. Sander, An algorithm for extracting the network geometry of three-dimensional collagen gels. *J. Microsc.* **232**, 463–475 (2008).
58. V. K. Lai, M. F. Hadi, R. T. Tranquillo, V. H. Barocas, A multiscale approach to modeling the passive mechanical contribution of cells in tissues. *J. Biomech. Eng.* **135**, 71007 (2013).
59. E. A. Sander, V. H. Barocas, R. T. Tranquillo, Initial fiber alignment pattern alters extracellular matrix synthesis in fibroblast-populated fibrin gel cruciforms and correlates with predicted tension. *Ann. Biomed. Eng.* **39**, 714–729 (2011).
60. H. Zhao *et al*., Fabrication and physical and biological properties of fibrin gel derived from human plasma. *Biomed. Mater.* **3**, 015001 (2008).